Monte Carlo simulation and analytical calculation of coherent bremsstrahlung and its polarisation

F.A. Natter [a], P. Grabmayr [a,*], T. Hehl [a], R.O. Owens [b], S. Wunderlich [a]

[a] *Physikalisches Institut der Universität Tübingen, Auf der Morgenstelle 14, D-72076 Tübingen, Germany*
[b] *Department of Physics and Astronomy, Glasgow University, Glasgow G12 8QQ, Scotland, UK*

Abstract

Spectral distributions for coherent and incoherent bremsstrahlung produced by electrons on thin diamond radiators are calculated accurately by a Monte Carlo procedure. Realistic descriptions of the electron beam and the physical processes within the radiator have been implemented. Results are compared to measured data. A faster calculation at only a slight loss of precision is possible using analytical expressions which can be derived after simplifying assumptions.
© 2003 Elsevier B.V. All rights reserved.

1. Introduction

Polarisation and asymmetry measurements play an increasingly important role in medium energy physics and have been instrumental in recent progress. In particular tagged beams of polarised photons have been employed for investigations of nucleon and nuclear structure. In order to minimise systematic errors in the interpretation of asymmetries from such measurements it is important to determine the photon polarisation as ac-curately as possible. This paper deals with the production of polarised photons by coherent bremsstrahlung in a crystal in which the regular structure of the atoms within a coherence volume enhances the radiation of polarised photons at certain energies. Since a satisfactory online monitor has not yet been developed, the polarisation must be deduced from the shape of the bremsstrahlung spectrum itself. The calculation of the spectrum is the subject of this paper.

The cross section for production of bremsstrahlung in a crystal (cr) is composed of coherent (co) and incoherent (in) parts, $\sigma^{cr} = \sigma^{co} + \sigma^{in}$, where σ is used as an abbreviation for the cross section differential in one or more of the kinematic variables. The incoherent cross section differential in photon energy k has a smooth, approximately

---
* Corresponding author. Tel.: +49-7071-297-4450; fax: +49-7071-29-5373.

E-mail address: grabmayr@uni-tuebingen.de (P. Grabmayr).

$1/k$, energy dependence while the coherent cross section exhibits structures related to the periodicities of the lattice. This is illustrated in Fig. 1(a) and (b) which show a smooth spectrum from an amorphous nickel radiator and a measured bremsstrahlung spectrum from a diamond radiator, respectively. The former has a shape similar to the incoherent part of the diamond spectrum. The coherent part can be decomposed into two contributions, $\sigma^{\mathrm{co}} = \sigma_\perp + \sigma_\parallel$, whose photon polarisation vectors are perpendicular ($\perp$) and parallel ($\parallel$) to the orientation of a reference plane defined by the incoming electron and the lowest reciprocal lattice vector of the crystal. Their difference σ^{dif} determines the photon beam polarisation P:

$$P = \sigma^{\mathrm{dif}}/\sigma^{\mathrm{cr}} = (\sigma_\perp - \sigma_\parallel)/\sigma^{\mathrm{cr}}$$
$$= \frac{\sigma_\perp - \sigma_\parallel}{\sigma_\perp + \sigma_\parallel}\left(1 - \frac{1}{R}\right), \quad (1)$$

where $R = \sigma^{\mathrm{cr}}/\sigma^{\mathrm{in}}$. Clearly P is affected by both the intrinsic polarisation of the coherent process and by the ratio R of the crystal and the inco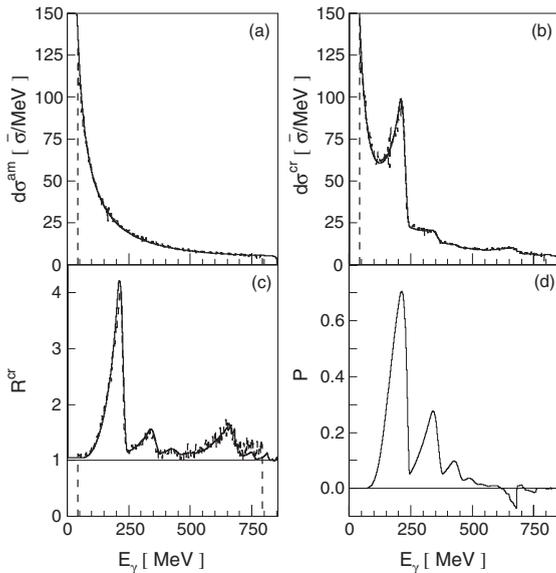herent cross sections. Since both the cross sections and the polarisation are obtained from the same calculation, it is argued here that the polarisation will be reliably determined, if the calculation describes correctly the detailed structure and relative intensities of all the measured spectra. This includes a check of the correct treatment of the incoherent contribution which has in general been measured using a different amorphous radiator, e.g. a thin nickel foil replacing the diamond crystal.

Evidently it is very important to reach the best possible description for the bremsstrahlung spectrum. This is not an easy task, because different radiators, electron beam divergence, a finite beam spot size, multiple scattering in the target and the effect of collimation all need to be modelled correctly.

Many years after the first suggestion by Williams [1], systematic work on coherent bremsstrahlung at relativistic energies was started by Überall [2]; this was continued by Diambrini Palazzi [3] and coworkers at Frascati and by Timm [4] at DESY. More recently Lohmann [5] and Rambo [6], later referred to as LR, took up this subject in connection with real photon experiments employing the Glasgow tagging spectrometer [7] at the cw electron accelerator MAMI [8] at Mainz. The basic treatments of polarisation in incoherent bremsstrahlung on single atoms were developed by May [9] and Maximon et al. [10].

The present paper builds on previous work mentioned above (and references therein) where the Bethe–Heitler bremsstrahlung formalism [11] is the common starting point. However, some approximations made by LR have been significantly improved in the present work. In particular, taking account of the energy and Z dependence of the angular distribution for the incoherent cross section, which was not done in LR, leads to changes of up to $\approx 10\%$ in R and P, depending on kinematics. An improved representation of the atomic form factor is used and the electron–electron bremsstrahlung is also treated in a more sophisticated way, which again changes the magnitude of R. The treatment of photon collimation has also been improved. For the simple case of a circular collimator an analytical collimation function is derived and the two-dimensional integral of the coherent intensity over electron beam divergence is

Fig. 1. Predictions obtained with the analytical code are compared to measured bremsstrahlung spectra, (a) σ^{am} for a 4 μm nickel radiator, (b)–(d) σ^{cr}, R^{cr} and P for a 100 μm diamond. The electron beam energy is 855 MeV.

replaced by an analytical approximation. Together these approximations enable rapid calculations using an analytic code. In order to take full account of all experimental factors such as an off-axis or tilted collimator with a finite length or a non-spherical beam profile and to avoid any of the above approximations, a Monte Carlo program has been written. In contrast to previous work, both codes include also a proper treatment of the beam energy spread.

Section 2, which presents the most important relations describing the bremsstrahlung process in a crystal, is based in particular on earlier work [4–6,9]. A general discussion of the new features implemented in the present calculations (Section 3) and a description of the two calculational methods (Section 4) are followed by a comparison of the calculations with measurements (Section 5).

2. The bremsstrahlung process in a crystal

2.1. General considerations

Bremsstrahlung is created when fast electrons interact with an electromagnetic field, in particular with a charge. The incoming electron with energy and momentum $(E_0, \vec{p}_0)$ emerges with $(E, \vec{p})$ creating a photon $(k, \vec{k})$ by transferring a small amount of momentum $\vec{q}$ to a third partner (usually an atomic nucleus of charge Z). The kinematics of the process is shown in Fig. 2 where the notation follows that of [5,6]. In this paper this process is treated in the extreme relativistic limit and the nuclear recoil energy is neglected, thus energy and momentum conservation yield $(E_0, \vec{p}_0) = (E + k, \vec{p} + \vec{k} + \vec{q})$. Natural units $(m_0 = c = \hbar = 1)$ are used and in appropriate cases the electron mass m_0 is neglected. The decomposition of the momentum transfer $\vec{q}$ into longitudinal q_l and transverse q_t components with respect to $\vec{p}_0$ permits the formulation of limits in their values which depend on the relative photon energy $x = k/E_0$:

$$\frac{\delta}{x} \geqslant q_l \geqslant q_l^{\min} = \delta + \frac{q_t^2}{2E_0}, \tag{2a}$$

$$1 \gtrsim q_t \geqslant 0, \tag{2b}$$

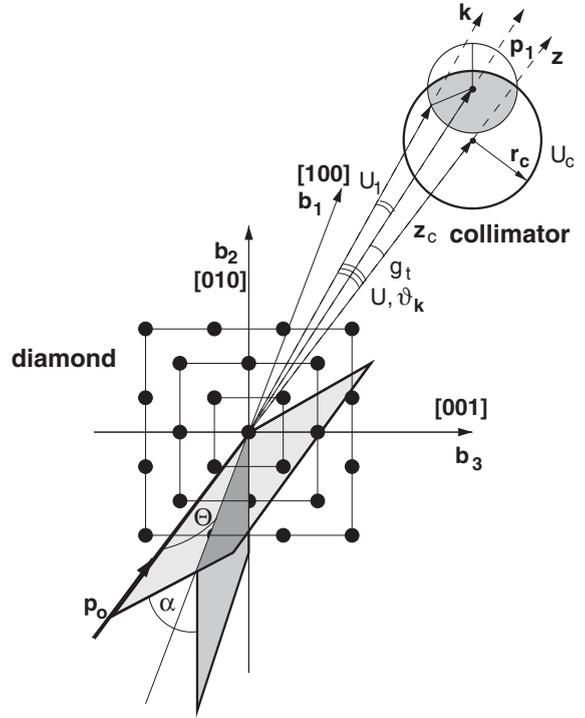

Fig. 2. The kinematics of the bremsstrahlungs process on a diamond crystal. The vectors and angles for the incoming electron $(\vec{p}_0 \| \vec{z})$, the outgoing electron $(\vec{p}_1)$ and the photon $(\vec{k})$ are shown. In addition the reduced angles g_t, U, U_1 and U_c are indicated at the appropriate positions. See also the tables and Fig. 11 of [6].

with

$$\delta = \frac{x}{2E_0(1-x)}. \tag{2c}$$

The lower limits are of kinematical origin and the upper limits are due to the rapid decrease of the cross section with increasing q. Often the upper limit in Eq. (2a) is simplified to $q_l \lesssim 2\delta$ with the simple assumption of $x \approx 0.5$. This allowed momentum transfer region is referred to as the 'pancake' due to its large transverse extension relative to the tiny longitudinal component.

2.2. The effect of the crystal

When the bremsstrahlung cross section is calculated without the summation over the photon polarisation [12–14], then in the low-energy limit the result obtained is

$$\frac{\mathrm{d}\sigma}{\mathrm{d}k} \propto \frac{1}{k}\cos^2\xi, \tag{3}$$

where ξ is the azimuthal angle of the polarisation vector $\vec{\epsilon}$ around $\vec{p}_0$ with respect to the plane $(\vec{p}_0, \vec{q})$, i.e. the maximum linear polarisation is found in the plane $(\xi = 0)$ defined by the momentum transfer.

When an electron scatters from a single atom producing incoherent bremsstrahlung the momentum transfer $\vec{q}$ may lie anywhere inside the pancake, leading to a uniform azimuthal distribution of the polarisation vector $\vec{\epsilon}$ and hence to an unpolarised photon beam. When produced on a crystal, however, the regular structure of the crystal described by the reciprocal lattice basis-vectors $\vec{b}_k$ restricts the magnitude and direction of the momentum transfer and thus the azimuth of the $(\vec{p}_0, \vec{q})$ plane. The only allowed values of the momentum transfer $\vec{q}$ are those which coincide with a reciprocal lattice vector $\vec{g} = \sum_{k=1}^{3} h_k \vec{b}_k$ for a given set of Miller indices $h_k = [h_1, h_2, h_3]$. The recoil can be absorbed by a large region within the lattice and the contributions of these atoms add coherently in the bremsstrahlung process, thus enhancing the yield. As $\vec{g}$ fixes $\vec{q}$ and the photon polarisation vector tends to lie dominantly in a single plane, a photon beam with large polarisation can be produced.

When coherent radiation is produced in a crystal, the momentum transfer components g_l and g_t for each contributing reciprocal lattice vector are fixed by the crystal orientation. As the relative photon energy x is increased, the longitudinal momentum transfer at the lower edge of the pancake $q_l^{\min}$ increases monotonically until it exceeds g_l (Eqs. (2a) and (2c)). This leads to a discontinuity in the photon spectrum at the corresponding energy x_d given in Eq. (4a).

$$x_d = (1 + 1/(2E_0 g_l - g_t^2))^{-1}, \tag{4a}$$

with

$$g_l = g_1 \cos\Theta + (g_2 \cos\alpha + g_3 \sin\alpha)\sin\Theta \tag{4b}$$

and

$$g_t^2 = (g_1^2 + g_2^2 + g_3^2) - g_l^2 = g^2 - g_l^2, \tag{4c}$$

where g_k, with $k = 1, 2, 3$, are the components of $\vec{g}$ in the crystal frame. The orientation of the crystal

$\underline{\Omega} = (\Theta, \alpha)$ with respect to the electron beam axis is defined as in [5,6,13].

The incoherent contribution remains almost constant across the discontinuity, while the coherent strength and thus the polarisation are both much larger just below it (see Fig. 1(b) and (d)). Therefore, this photon energy region is the interesting one for the production of a polarised photon beam.

2.3. The bremsstrahlung cross section

The 5-fold differential cross section σ^{cr} for bremsstrahlung production on a crystal [4,9] has a main term related to the cross section σ^{am} for electron–nuclear bremsstrahlung from an amorphous sample of the same material and a smaller term which accounts for bremsstrahlung from the atomic electrons σ^{el}, which was omitted in the previous discussion.

$$\begin{aligned}
\sigma^{\mathrm{cr}} = &\left[\frac{1}{N_{\mathrm{cell}}} \left(\frac{2\pi}{a} \right)^3 \sum_{\vec{g}} |S(\vec{g})|^2 \delta_{\mathrm{D}}(\vec{q} - \vec{g}) \cdot f_{\mathrm{DW}}(q^2) \right. \\
&\left. + (1 - f_{\mathrm{DW}}(q^2)) \right] \sigma^{\mathrm{am}} + \sigma^{\mathrm{el}} \\
= &\; \sigma^{\mathrm{co}} + \sigma^{\mathrm{in}} + \sigma^{\mathrm{el}}, \tag{5}
\end{aligned}$$

where δ_{D} is the Dirac delta function, $\sigma^{\mathrm{am}} = (1 - F^e(q^2))^2 \sigma^{\mathrm{un}}$ and σ^{un} is the cross section for an unscreened nucleus.

The factor $S(\vec{g})$ describes the interference of the coherent amplitudes from the N_{cell} atoms of the unit cell, whose volume is a^3. The atomic form factor $F(q^2) = (1 - F^e(q^2))$ accounts for the screening of the nuclear charge by the charge distribution of the surrounding electrons. The Debye–Waller factor $f_{\mathrm{DW}}(q^2)$, which depends on the temperature and crystal properties, describes the influence of thermal motion in smearing out the periodicity of the lattice and gives the fraction of the atoms which radiate coherently. The remaining fraction $(1 - f_{\mathrm{DW}}(q^2))$ produces incoherent radiation.

A single differential cross section is obtained by integrating Eq. (5). It is usually multiplied by $x/\bar{\sigma}$ to obtain a dimensionless photon intensity I per atom. The latter and the polarisation P can be

expressed in terms of the functions $\Psi_{1,2,3}^j$ with $j = \{\text{co, in and el}\}$:

$$I^j = \frac{x}{\bar{\sigma}}\frac{\mathrm{d}\sigma^j}{\mathrm{d}x} = (1 + (1-x)^2)\psi_1^j - \frac{2}{3}(1-x)\psi_2^j, \quad (6a)$$

$$P = I^{\mathrm{dif}}/I^{\mathrm{cr}} = 2(1-x)\psi_3/(I^{\mathrm{co}} + I^{\mathrm{in}} + I^{\mathrm{el}}), \quad (6b)$$

where $\bar{\sigma} = \alpha^2 Z^2 = 0.57947 \cdot Z^2$ mb.

The functions ψ^{co} are given below:

$$\psi_1^{\mathrm{co}} = 4\sum_{\vec{g}} G(\vec{g})\delta g_t^2 g_1^{-2}, \quad (7a)$$

$$\psi_2^{\mathrm{co}} = 24\sum_{\vec{g}} G(\vec{g})\delta^2(g_1 - \delta)g_t^2 g_1^{-4}, \quad (7b)$$

$$\psi_3^{\mathrm{co}} = -4\sum_{\vec{g}} G(\vec{g})\delta^3 g_1^{-4}$$
$$\times [(g_2^2 - g_3^2)\cos 2\phi + 2g_2 g_3 \sin 2\phi] \quad (7c)$$

and

$$G(\vec{g}) = \frac{(2\pi)^2}{a^3 N_{\mathrm{cell}}} f_{\mathrm{DW}}(g^2)|S(\vec{g})|^2 F_r^2(g^2)g^{-4}.$$

The angle ϕ is defined as the angle between the reference plane $(\vec{b}_1, \vec{e}_x)$ and the crystal plane $(\vec{b}_1, \vec{b}_2)$, and it is the azimuthal angle of the polarisation vector $\vec{\epsilon}$ (see [6]). For the coherent cross section the atomic form factor $F_r(q^2) = (1 - F_r^e \times (q^2))$ is obtained using a realistic electron charge distribution from a Hartree–Fock calculation for carbon. The details are given in Section 3.1, where the changes compared to the earlier calculations of LR are also discussed.

The incoherent part of the angle-integrated spectrum from a diamond can be represented very accurately, except near its upper end point, by Eq. (6a) with constant values for $\psi_1^{\mathrm{in}} = 13.79$ and $\psi_2^{\mathrm{in}} = 13.12$. These values are obtained from integrals in Eq. (3BS(b)) of [15] using a Hartree–Fock form factor and including the Debye–Waller factor. However, it is also important to account accurately for the angular dependence of the spectrum shape; this is discussed in Section 3.3.

In treating the electron bremsstrahlung cross section σ^{el}, LR rely on a Thomas–Fermi model screening calculation by Wheeler and Lamb [16], which yields the constant values $\psi_1^{\mathrm{el}} = 4.05$ and $\psi_2^{\mathrm{el}} = 3.94$. Improvements to this parameterisation will be presented in Section 3.4.

An amorphous nickel radiator was employed here to obtain a smooth reference spectrum, which has served as substitute for the incoherent part when no calculation was available, and which is used to remove unwanted fluctuations in the spectrum from the diamond caused by efficiency variations in the detectors of the tagging spectrometer. The standard practice, also adopted by LR, of using the Thomas–Fermi model to evaluate the atomic form factor, was followed for the calculation of nuclear bremsstrahlung, but modified to include the improved parameterisations of the electron–nuclear and electron–electron bremsstrahlung discussed in other sections. However, in Section 5.2 we suggest an improved method which reduces systematic uncertainties from the calculations and avoids experimental normalisation problems, which ensue when two different radiators are used.

2.4. The angular distribution of the photons

It is important that the photon angular distribution is treated accurately since of necessity the photon beam is collimated. In fact collimation can be used to enhance the photon polarisation by taking advantage of the differences in the angular distributions of the coherent and incoherent processes.

Unfortunately, there is no treatment available for the angular distribution of σ^{am} based on realistic atomic screening which reaches beyond an atomic form factor of dipole type. In momentum space the dipole form factor represents the Fourier transform of the exponentially screened Coulomb potential introduced by Schiff [21]. For a crystal the incoherent cross section σ^{in} is also affected by the Debye–Waller factor (see Eq. (5)) which further complicates the analytical evaluation. In this situation LR have resorted to a fairly radical approximation for the angular distribution of σ^{in}. They assume that the angular distribution of σ^{am} is independent of both Z and photon energy x and approximate the dependence on the photon polar angle ϑ_k by a form for which the fraction of the total intensity lying at angles below

the reduced angle $U = (E_0 \vartheta_k)$ is $f(U) = U^2/(1 + U^2)$. An improved approach is presented in Section 3.3.

For the coherent process the angular distribution is more complicated. The constraint on the momentum transfer, $\vec{q} = \vec{g}$, produces a direct relation between the photon energy x and its reduced angle U_1 with respect to the direction $\vec{p}_1 = \vec{p}_0 - \vec{g}$, in which the maximum photon energy x_d for the lattice vector $\vec{g}$ is found.

$$U_1^2 + 1 = \frac{1-x}{x} \frac{x_d}{1-x_d} = \frac{1-x}{x}(2E_0 g_1 - g_t^2). \qquad (8)$$

The direction $\vec{p}_1$ makes a small reduced angle g_t with the incident electron direction $\vec{p}_0$. Because the axis of the radiation cone has this angular offset, photons of a particular energy x are produced over a small range ($\leqslant 2g_t$) of angles U with respect to the electron direction. LR did not take account of the offset and obtain a slightly different relation between photon energy and angle, the effect of which is estimated in Section 3.2.

Since the energy of the coherent photons decreases with photon angle, collimation can be used to remove the low-energy tail of the coherent peak without affecting the intensity in the peak region itself. The photon polarisation in the peak region is therefore enhanced by collimation, since it simultaneously reduces the incoherent intensity at all photon energies and also removes the overlapping low-energy tails of the coherent peaks produced by higher lattice vectors. This was shown first in [17,18] and later in [6,13]. It is also found that when the beam is collimated the polarisation becomes especially sensitive to the finite phase space of the incident electron beam. These effects are treated in the next two sections.

3. Improvements in the present calculations

This section comprises a discussion of the main improvements made in the formulae used to evaluate the bremsstrahlung cross section viz. (i) the parameterisation of the carbon form factor, (ii) the angular distribution of the coherent electron–nuclear contribution, (iii) the angular distribution

of the incoherent electron–nuclear contribution and (iv) the parameterisation of the energy and Z dependence of the electron–electron bremsstrahlung.

Improvements were also made in the computational treatment of the effects of the finite phase space of the electron beam on the photon spectrum i.e. the spot size, angular divergence and energy spread of the electron beam, multiple scattering in the radiator and the photon collimation process. These are discussed along with other computational details in Section 4.

3.1. The carbon form factor

The shape of the form factor $F(q^2) = (1 - F^e(q^2))$ is important because its magnitude at different values of momentum transfer q influences both the coherent and the incoherent contributions to the cross section.

Timm [4] and LR [5,6] use a parameterisation of the carbon atomic form factor by Cromer and Waber [19], which however is valid only up to $q = 0.1$. For $q > 0.1$ Timm suggests that the decrease of $F^e(q^2)$ be approximated by the dipole form corresponding to a screening potential of exponential shape. However, LR do not adopt this approximation; they set $F^e(q^2) = $ const. for $q > 0.1$, which causes the incoherent cross section to be underestimated. The present work uses a parameterisation (Eq. (9)) of the form factor for a chemically bound carbon atom valid up to $q < 0.3$. This was taken from a more recent review by Maslen et al. [20]. For higher q the form factor is approximated by the dipole form matched at $q = 0.3$.

$$F_r^e(q^2) \cdot Z = \begin{cases} \sum_{i=0}^4 a_i \exp(-b_i q^2) & q < 0.1, \\ \exp(\sum_{i=0}^3 c_i q^i) & 0.1 < q \leqslant 0.3, \\ d_0/(1 + d_1 q^2) & q > 0.3, \end{cases}$$
$$(9)$$

$a_i = 0.286977, 2.26099, 1.56165, 1.05075, 0.839259;$
$b_i = 0, 9635.97, 278.863, 4143.12, 23609.3;$
$c_i = 1.7056, -32.3042, 50.5055, -37.3811;$
$d_i = 3.94323, 3731.46.$

3.2. The angular distribution of the coherent cross section

To determine the effect of collimation on the coherent spectrum, a relation between the photon energy x and its polar angle U with respect to the electron beam is required. Eq. (8) relates x to the angle U_1 with respect to $\vec{p}_1$ and the relation between U and U_1 is

$$U^2(x, \zeta) = U_1^2(x) + g_t^2 + 2U_1(x)g_t \cos \zeta, \tag{10}$$

where ζ is the azimuthal angle of the photon around the $\vec{p}_1$-direction. Averaging over this variation one obtains

$$\langle U^2(x) \rangle = U_1^2(x) + g_t^2$$
$$= \frac{1-x}{x} \frac{x_d}{1-x_d} + g_t^2 - 1. \tag{11}$$

When the coherent intensity is integrated over photon angles, the weak dependence of $U(x, \psi_k)$ on the photon angle ψ_k, which is the azimuthal angle between the $(\vec{p_0}, \vec{k})$ and the $(\vec{b_i}, \vec{p_0})$ planes, is ignored; the coupling between x and U in the contribution of each $\vec{g}$ to the triple differential cross section, and thus to the polarisation, is accounted for by a Dirac delta function δ_D:

$$\frac{\mathrm{d}^2 I^{\mathrm{co}}}{\mathrm{d}(U^2)\,\mathrm{d}\psi_k} = \left[(1 + (1-x)^2)\Phi_1 - \frac{2}{3}(1-x)\Phi_2 \right]$$
$$\times \delta_D(U^2 - \langle U^2(x) \rangle), \tag{12a}$$

$$P(U^2)\,\mathrm{d}\psi_k = \frac{2(1-x)\Phi_4(\psi_k)\delta_D(U^2 - \langle U^2(x) \rangle)}{(1 + (1-x)^2)\Phi_1 - \frac{2}{3}(1-x)\Phi_2}. \tag{12b}$$

The Φ functions are given in [6]. They are related to the Ψ^{co} functions via an integration over U^2 and ψ_k.

The photon intensity spectrum after collimation to the angle ϑ_c is

$$I^{\mathrm{co}}(U_c, x) = \int_0^{U_c^2} \mathrm{d}(U^2) \int_0^{2\pi} \mathrm{d}\psi_k \frac{\mathrm{d}^2 I^{\mathrm{co}}}{\mathrm{d}(U^2)\,\mathrm{d}\psi_k}$$
$$= I^{\mathrm{co}}(x) \cdot \Theta(x - x_c), \tag{13}$$

where $U_c = (E_0 \vartheta_c)$ and Θ is the Heavyside step function, which arises through the δ_D function in Eqs. (12). The Heavyside function incorporates the

photon energy–angle relationship (Eq. (11)), which removes photons of energy less than x_c, where

$$x_c = \left(1 + \frac{U_c^2 + 1 - g_t^2}{2E_0 g_1 - g_t^2} \right)^{-1}$$
$$= \frac{x_d}{1 + (U_c^2 - g_t^2)(1 - x_d)}. \tag{14}$$

Omitting the g_t terms in Eqs. (4a) and (14), as done by LR, causes a shift of x_c and x_d by typically 1% at electron beam energies of 855 MeV, the standard setting at the MAMI facility in Mainz. Because many different lattice vectors contribute to the total spectrum, individual variations of these discontinuities cause a distortion of the spectrum.

3.3. The angular distribution of the incoherent cross section

A good approximation to the angular and energy distribution from an amorphous radiator has been obtained by Schiff [21] and Hubbell [22] using an exponential screening potential, $(Ze/r) \exp(-rZ^{1/3}/C)$, which is equivalent to approximating the form factor F^e by the dipole form

$$F_d^e(C, q^2) = \left[1 + (qCZ^{-1/3})^2 \right]^{-1}. \tag{15}$$

The resulting photon intensity is

$$\frac{\mathrm{d}I^s}{\mathrm{d}(U^2)} = (1 + (1-x)^2)\Phi_1^S - \frac{2}{3}(1-x)\Phi_2^S, \tag{16a}$$

$$\Phi_1^S = 2v^2(M(v) - 1), \tag{16b}$$

$$\Phi_2^S = 6v^2(1 + (2M(v) - 8)(1-v)v) \tag{16c}$$

with

$$v = 1/(1 + U^2), \quad M(v) = -\ln\left[\frac{Z^{2/3}}{C^2}(\delta_z^2 + v^2) \right] \tag{16d}$$

and

$$\delta_z = \frac{C\delta}{Z^{1/3}}. \tag{16e}$$

The constant C was evaluated as $C = 111$ in [15, 22] by normalising the total bremsstrahlung intensity from the Schiff formula (Eq. (16)) to that predicted by the Bethe–Heitler cross section.
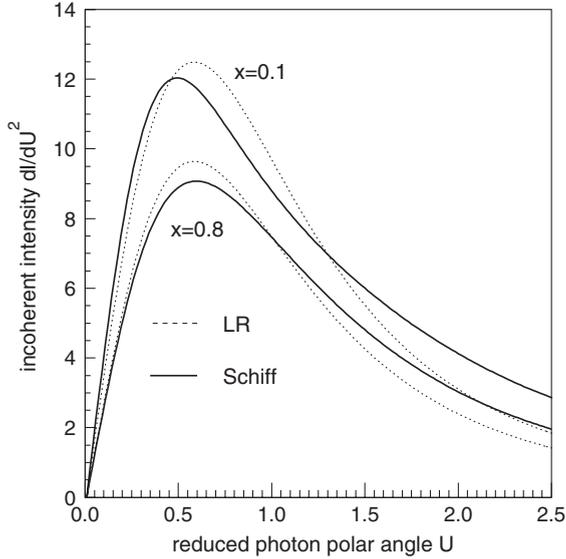
Fig. 3. The angular distribution of bremsstrahlung from amorphous carbon for two photon energies ($x = 0.1$ and 0.8): Schiff formula (Eq. (16) – solid line), LR approximation ($f(U) \times$ integrated-over-angle Bethe–Heitler intensity – dashed line). The angular distribution $f(U)$ is normalised to the Schiff intensity for comparison.

In Fig. 3 the Schiff formula is compared with the approximation used by LR, namely an angular distribution shape independent of photon energy multiplied by the integrated-over-angle Bethe–Heitler cross section. The comparison shows that this approximation does not adequately represent the cross section and it will necessarily produce errors in the calculation of the collimated intensity. Although the Schiff formula does not incorporate the realistic carbon form factor F_r, it should provide the basis for an improved treatment of I^{in} compared to that used by LR.

However, first it is necessary to take account of the effect of the Debye–Waller factor, which leads to an effective form factor $F(q^2)(1 - f_{DW}(q^2))^{1/2}$ in the incoherent process. The analytical integration over electron angles leading to the Schiff result is not possible with this modified form factor and therefore an approximate method of including the Debye–Waller factor was investigated [14].

This relied on using a modified screening constant C in the Schiff cross section to represent its effect. The values of C are found for which

$$\int \mathrm{d}\Gamma \, I_s(C) = \int \mathrm{d}\Gamma \, I_{BH}(1 - f_{DW})F_r^2, \qquad (17)$$

where $\mathrm{d}\Gamma = \sin \Theta_k \, \mathrm{d}\Theta_k \sin \Theta_e \, \mathrm{d}\Theta_e \, \mathrm{d}\phi$ and I_{BH} is the 5-fold differential cross section of Bethe–Heitler (Eq. (1BS) in [15]). The calculations were carried through using the Monte Carlo integration code VEGAS [23]. For a crystal at room temperature, the Schiff spectrum with $C = 30.4$ represented energy and angle dependence of the full calculation using the realistic form factor and including the Debye–Waller factor to better than 0.5%. The Schiff spectrum with modified C is computationally convenient and was used in all subsequent calculations. The effect of the temperature dependence of the Debye–Waller factor was determined and it was found that the temperature of the diamond, $T(K)$, can be taken into account using a temperature dependent screening constant $C = 27.24 + 0.0108 T/K$.

The form factor and the effect of the Debye–Waller factor are shown in Fig. 4. The arrows indicate the momentum transfers in a diamond radiator responsible for the two most prominent peaks in the coherent spectrum. The realistic form factor F_r is not well represented by the approximate form F_d suggested by Schiff when using the standard value $C = 111$ [21]. However, by using the value $C = 71$ as suggested by Timm [4] a good fit can be obtained at the higher q values which are of importance in calculating the incoherent spectrum, although the Debye–Waller effect is not included. The lower part of the figure shows the reduction due to this factor, $(1 - f_{DW})$. One sees that the dipole form factor with $C = 35$ describes the realistic form $(1 - f_{DW})F_r^2$ reasonably well.

To visualise the influence of the form factors on the amorphous and incoherent cross sections, weighting functions suggested in [15],

$$w_q(q) = \frac{\mathrm{d}}{\mathrm{d}q} \left(\frac{\mathrm{d}\sigma^{3BSb}}{\mathrm{d}x} \right), \qquad (18)$$

have been calculated and are presented in Fig. 5. These point out the relative importance of different regions of q in the integrals which determine the cross section over a much larger q-range than shown in Fig. 4. The average q values contributing to the integrals (at Mainz energies) are marked by
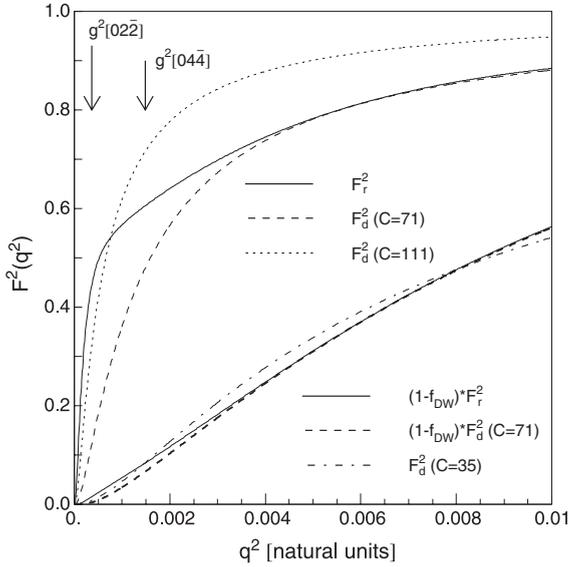
Fig. 4. The ^{12}C realistic form factor from [20] is compared to the dipole form factor which was calculated with a screening constant of $C = 111$ from a Thomas–Fermi model [21] and with $C = 71$ as suggested by Timm [4]. The Debye–Waller factor suppresses the form factor significantly at low q-values, which are of little importance for the incoherent cross section (see Fig. 5). To model the total form factor $F_{tot}^2(q^2) = (1 - f_{DW})F_r^2$, an effective dipole form factor with a temperature dependent screening constant $C = 35$ was used. The arrows indicate the relevant momentum transfer for the two dominant contributions arising from the $[0\,2\,\bar{2}]$ and $[0\,4\,\bar{4}]$ vectors.
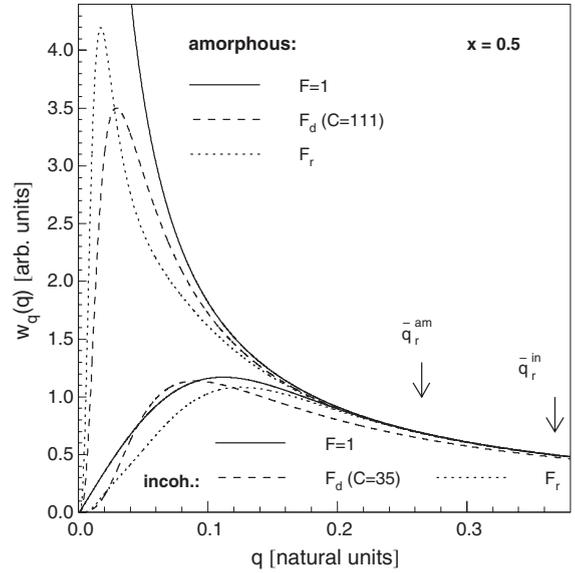

Fig. 5. Distribution of the contributions to the bremsstrahlung intensity at photon energy $x = 0.5$ as a function of momentum transfer for an unscreened nucleus ($F = 1$) and for two form factors, both (dipole and realistic) shown with and without the inclusion of the Debye–Waller factor. The mean values of the momentum transfer are also shown for the realistic form factor to illustrate the suppression of small values of momentum transfer for incoherent bremsstrahlung compared to the amorphous case.

arrows in Fig. 5, which demonstrate that, as a result of the Debye–Waller factor, the mean q-value for the incoherent process in diamond is significantly higher than that for amorphous carbon.

A convenient feature of the Schiff cross section (Eq. (16)) is the availability of an analytic form [22] integrated over photon angle up to a maximum angle $U = E_0\vartheta$, which can be the collimator angle U_c. The result in terms of $v = 1/(1 + U^2)$, which is used in the present calculations, is

$$\Psi_1^S = 2[1 + M(1) - (1 + M(v))v - c], \qquad (19a)$$

$$\Psi_2^S = -\frac{40}{3}v^3 + 18v^2 - (8\delta_z^2 + 6)v + 8\delta_z^2$$

$$+ 2M(1) + \frac{4}{3} + (4v^3 - 6v^2)M(v)$$

$$- 6\delta_z^2\left(M(v) - M(1) + \frac{2}{3}c\right), \qquad (19b)$$

with

$$c = 2\delta_z \arctan\left(\frac{1 - v}{\delta_2 + v/\delta_z}\right). \qquad (19c)$$

These functions can represent either amorphous or incoherent intensities depending on the screening constant C entering M and δ_z (see Eq. (16)).

In Fig. 6 the photon intensity spectra within different collimation angles U_c are displayed, normalised to unit area to allow better comparison of their shapes. The non-trivial dependence of the intensity on the collimation angle is poorly described by an energy-independent reduction factor $f(U_c)$. The use of the latter would lead to an incorrect collimated incoherent intensity, and hence to an inaccurate polarisation.

3.4. The electron–electron bremsstrahlung

In experiments the shape of the photon spectrum produced on an amorphous nickel radiator is
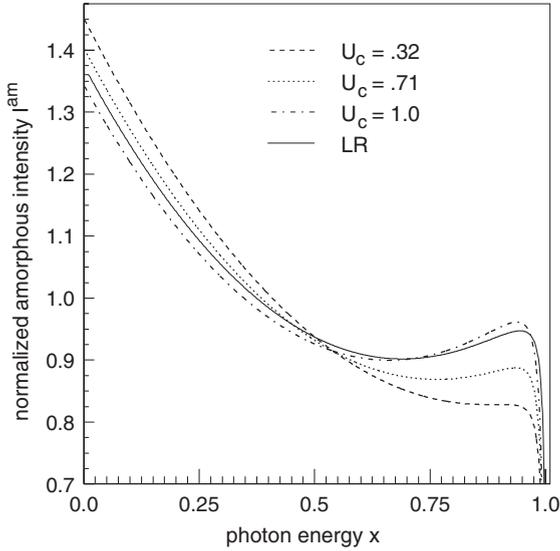
Fig. 6. Comparison of intensity spectra from Eq. (19) for $Z = 6$ and $C = 35$ for different collimation angles U_c with the LR treatment: $\sigma(x, U_c) = \sigma_{BH}(x)f(U_c)$. The integrated intensities are normalised for comparison.

measured and used to remove the main photon energy dependence of spectra from the diamond radiator. Because the relative contribution of electron–electron bremsstrahlung is significantly different for the two radiators, it is important that its energy and Z dependence is properly accounted for. Formulae for Ψ_1^{el} and Ψ_2^{el} are taken from [15]. They are based on the Thomas–Fermi model using the extreme relativistic approximation, but do account for the atomic electron binding.

$$\Psi_1^{el} = \frac{1}{Z}\left[\psi(\epsilon) - 4 - \frac{8}{3}\ln Z\right] = \Psi_2^{el} - \frac{2}{3Z}, \qquad (20a)$$

$$\psi(\epsilon) = \begin{cases} 19.19 - 4\ln\epsilon & \text{for } \epsilon \geqslant 0.88, \\ \sum_{n=0}^{5} e_n(0.88 - \epsilon)^n & \text{for } \epsilon < 0.88, \end{cases} \qquad (20b)$$

with

$$\epsilon = \frac{100}{E_0 Z^{2/3}}\frac{x}{1 - x}$$

and

$$e_n = 19.7, 4.177, -3.806, 31.84, -58.63 \text{ and } 40.77.$$

The parameterisation of $\psi(\epsilon)$ is taken from [24].

4. The improved calculations and the codes

Up to now an ideal electron beam and a thin radiator was assumed, which cannot be realized in actual experiments. Realistic beams are extended and divergent and the radiators have finite thickness, therefore the respective distributions and side effects must be accounted for in proper modelling. The coherent contribution is more affected by the experimental conditions than the incoherent one, especially when the beam is collimated [6,13,17], and the following discussion emphasises this case.

It is expected, that variations of the yield calculated for realistic cases will be due mainly to changes in polar and azimuthal angles with respect to the beam axis z. Since the characteristic angle is $1/E_0$ (typically of the order of mrad) and the angle changes are also small, the small-angle approximation is valid. This simplifies the transformation between the crystal and the (incident) electron coordinate system and allows the distributions to be defined in terms of vectors in the (x, y) plane perpendicular to the beam axis.

The angular divergence of the electron beam (BD), described by $w_{BD}(\underline{a})$ smoothes the discontinuity at x_d, because the crystal orientation with respect to the electron direction varies from its nominal setting $\underline{\Omega}$ in the laboratory system. This in turn changes the photon intensity due to the dependence of the momentum transfer on the crystal angles. It also smoothes the lower discontinuity at x_c in the collimated spectrum (see Eq. (14)), because the photon cone is no longer centred on the collimator. The beam angular distribution w_{BD} is assumed to be of Gaussian shape with variances σ_{ax} and σ_{ay}, in horizontal and vertical direction:

$$w_{BD}(\underline{a}) = w_{BD}(a_x, a_y)$$
$$= \frac{1}{2\pi\sigma_{ax}\sigma_{ay}}\exp\left(-\frac{a_x^2}{2\sigma_{ax}^2} - \frac{a_y^2}{2\sigma_{ay}^2}\right). \qquad (21)$$

The vector $\underline{a}$ denotes the transverse components of a unit direction vector, which together with the momentum describes the initial electron before reaching the radiator. This and other underlined vectors are used to describe directions and changes

of directions and to represent also the respective polar and azimuthal angles.

The overall angular spread of the electrons is further increased by multiple small-angle Coulomb scattering (MS) while traversing the radiator of thickness z_R. For scattering in an amorphous material the Molière theory [25,26] describes the distribution $w_{MS}(\underline{m}, z)$ of $\underline{m}$, the transverse component of the direction vector which the electron acquires due to multiple scattering after reaching a depth z inside the radiator. In the present calculations the distribution is approximated by Gaussians with variances $\sigma_{mx} = \sigma_{my} = \sigma_m$.

For electrons incident on a crystal at a very small angle to a crystal axis, Akhiezer et al. [27] have shown that the angular width of the multiple scattering distribution is increased due to coherent scattering by several neighbouring atoms along the atomic string. By scaling the results given in [27] for a silicon crystal, it is estimated the increase for electrons incident at an angle Θ to the $\langle 0\,0\,1 \rangle$ axis of a diamond will be a factor $f \approx 5[\Theta \ (\text{mrad})]^{-1/2}$ applicable in the region $0.25 \leqslant \Theta \leqslant 2$ mrad. When using the 855 MeV electron beam at Mainz to produce coherent bremsstrahlung, a setting $\Theta \approx 60$ mrad is used (see also [5]). At this setting the increase should be negligible, although the extrapolation is too large to allow a definite conclusion. However, the increase may become significant for higher energy beams, since the appropriate crystal alignment varies as $\Theta \sim 1/E_0$. For a 6 GeV beam at the Jefferson Laboratory this would lead to $f \sim 1.8$, which will produce a significant smearing of the coherent breamsstrahlung peak. A more detailed investigation of the coherent scattering process would clearly be of value for applications at such energies.

A finite electron beam spot size (BS) on the radiator has the same effect as a collimator with a fuzzy edge: both produce a smeared cut-off in the photon spectra at x_c. The assumed form of the beam spot distribution $w_{BS}(\vec{s})$ is the same as w_{BD} but with variances σ_{sx} and σ_{sy}, respectively.

Finally, structures in the coherent bremsstrahlung spectrum are also broadened by the electron beam energy spread (ES) around the nominal energy E_0, which is parameterised by the distribution $w_{ES}(\tilde{E}_0)$, again with assumed Gaussian shape

$$w_{ES}(\tilde{E}_0) = \frac{q}{\sqrt{2\pi\sigma_E^2}} \exp\left(-\frac{(\tilde{E}_0 - E_0)^2}{2\sigma_E^2} \right). \qquad (22)$$

The experimental photon intensity results from folding of all these effects weighted with the appropriate distributions. Usually a collimator with radius r_c is situated at distance z_c to define the photon flux on the experimental target. Due to the complicated dependence of $\vec{r}_\gamma$ of the produced bremsstrahlung photon on all integration variables of Eq. (23), the collimation condition for photons passing through the collimator $r_\gamma < r_c$ leads to topologically non-trivial integration limits.

$$
\begin{aligned}
I_c^{exp} = \frac{1}{z_R} \int_{ES} \mathrm{d}\tilde{E}_0 \int_{BS} \mathrm{d}^2 s \int_0^{z_R} \mathrm{d}z \int_{MS} \mathrm{d}^2 m \\
\times \int_{BD} \mathrm{d}^2 a \, w_{ES}(\tilde{E}_0) w_{BS}(\vec{s}) w_{MS}(\underline{m}, z) w_{BD}(\underline{a}) \\
\times \left. I^{co}(\underline{\Omega}, \underline{e}(\underline{a}, \underline{m})) \right|_{r_\gamma < r_c}.
\end{aligned}
\qquad (23)
$$

Note, that the evaluation of the coherent contribution I^{co} accounts for the crystal orientation and the actual electron direction $\underline{e}$ at the time of interaction. It is evident that the evaluation of this integral calls for a Monte Carlo treatment.

4.1. Description of the Monte Carlo program MCB

The Monte Carlo method is well established for simulation of complex processes in nuclear physics. Eq. (23) with its interrelated boundary conditions is an excellent example. Measured electron beam parameters and their standard deviations as well as radiator and collimator properties are the basic input. For each incoming electron, a particular set of physical values is chosen randomly in the parameter space appropriate for the investigation. First the energy $\tilde{E}_0$, hence the momentum of the incident electron, its impact position $\vec{s}$ and direction $\underline{a}$ are chosen from the Gaussian distributions defined previously, and its polar and azimuthal angles, θ_a and ϕ_a, with respect to the ideal beam direction $\vec{p}_0$ and the $(\vec{p}_0, \hat{z})$ plane are obtained. The depth z of the bremsstrahlung process inside the radiator is then taken from a uniform distribution within the radiator thickness z_R,

because the attenuation of the beam inside the radiator is still negligible. The width σ_m of the multiple scattering angular distribution is determined at this depth and the multiple scattering angles $\underline{m}(\theta_m, \phi_m)$ are chosen next: θ_m from the Gaussian distributions $w_{MS}(\underline{m}, z)$ and ϕ_m from a uniform distribution. The electron eventually obtains the final incidence angle $\underline{e}(\theta_e, \phi_e) = \underline{a} + \underline{m}$, which is then given by

$$\theta_e^2 = \theta_a^2 + \theta_m^2 + 2\theta_a\theta_m \cos\phi_m, \tag{24a}$$

$$\phi_e = \phi_a + \arcsin(\theta_m \sin\phi_m/\theta_e), \tag{24b}$$

since the small-angle approximation can be used for all polar angles.

To calculate the coherent cross section for the chosen electron parameters it is mandatory to find the crystal orientation $\underline{\Omega}_e(\Theta_e, \alpha_e)$ with respect to the actual electron direction $\underline{e}$, which is chosen from the distributions of beam divergence and then modified by the multiple scattering at the chosen depth within the crystal. This is related to the crystal orientation $\underline{\Omega}(\Theta, \alpha)$ in the laboratory system by $\underline{\Omega}_e = \underline{\Omega} + \underline{e}$ or

$$\Theta_e = \sqrt{\Theta^2 + \theta_e^2 + 2\theta_e\Theta \cdot \cos(\phi_e - \phi - \alpha)}, \tag{25a}$$

$$\alpha_e = \alpha + \arcsin(\theta_e \sin(\phi_e - \phi - \alpha)/\Theta_e). \tag{25b}$$

The angles of the produced photon are described by $\underline{\gamma} = (\theta_k, \phi_k)$ in the laboratory system, which is obtained from the emission angle in the electron system $\underline{\gamma}_e$ by $\underline{\gamma} = \underline{\gamma}_e - \underline{e}$.

Next, a lattice vector is chosen randomly from the set, which spans the volume of reciprocal space $V_{\vec{g}} = \prod_{k=1}^{3}(2h_k^{max} + 1)$ up to the Miller indices h_k^{max}. The coherent cross section $I^{co}(\vec{\Sigma})$ e.g. is calculated with this parameter vector $\vec{\Sigma} = (h_1, h_2, h_3, \underline{\Omega}, \underline{m}, s, z, \underline{\gamma}, \underline{a}, x)$. The cross section is differential in photon energy and both photon angles, the azimuthal angle ϕ_k and the polar angle ϑ_k.

The calculation of Eq. (23) is carried out by a Monte Carlo procedure (see [23]). Accepted parameter vectors $\vec{\Sigma}$ are stored in list mode for subsequent plotting or further investigations. In addition a key is also stored, indicating whether the emitted bremsstrahlung photon satisfies the condition for acceptance by the collimator, viz.

$$\left. \begin{array}{l} r_\gamma(z = z_c) < r_c \\ r_\gamma(z = z_c + l_c) < r_c \end{array} \right\} \quad \text{with } r_\gamma(z) = |\vec{s} + z\underline{\gamma} - \vec{s}_c|. \tag{26}$$

Here r_c, z_c and l_c denote the radius, the distance to the radiator and the length of the collimator, respectively. As seen from the above formulae an ideal collimator is assumed without any rescattering of the photons. A misalignment of the collimator by $\vec{s}_c$ is accounted for by an equivalent shift of the beam spot.

For the incoherent case the same procedure is applied and the same parameter sets are employed. Finally, standard analysis software such as PAW or ROOT is used to process the various list-mode data and to combine them for histogramming of the final spectra.

4.2. Description of the ANalytical Bremsstrahlung code (ANB)

The calculation of the photon energy dependence of the polarisation with full consideration of all experimental conditions by the Monte Carlo method outlined above is very time consuming. The procedure can be accelerated drastically by applying some approximations to obtain an analytical expression for this 8-fold integral. This approach (ANB) is useful in particular for survey studies. For results with full precision and without any approximations, the Monte Carlo version (MCB) can be run subsequently with parameters in the neighbourhood of the optimal set found by ANB.

The following approximations are applied to derive an analytical expression for Eq. (23):

(i) All two-dimensional transverse distributions are assumed to be Gaussian in shape with azimuthal symmetry. For example, the beam angular distribution (BD) becomes

$$w_{BD}(a_x, a_y) = \frac{1}{2\pi\sigma_a^2} \exp\left(-\frac{1}{2\sigma_a^2}\left(a_x^2 + a_y^2\right)\right), \tag{27}$$

where $\sigma_a^2 = \sigma_{ax}\sigma_{ay}$.

(ii) A mean multiple scattering (MS) variance $\overline{\sigma}_m^2$ is obtained from the variance $\sigma_m^2(z)$ averaged over the crystal thickness.

(iii) An overall electron angular distribution $w_{ED}(\underline{e})$ with variance $\sigma_e^2 = \sigma_a^2 + \overline{\sigma}_m^2$ is obtained by folding the MS and BD distributions.

(iv) For the calculation of the collimated photon spectrum, the effects of the beam spot size, beam divergence and multiple scattering are combined into a Gaussian angular distribution $w_{CB}(\rho)$ with variance $\sigma_c^2 = \sigma_e^2 + \sigma_{sx}\sigma_{sy}/z_c^2$. This distribution represents the angular offset of the centre of the photon cone with respect to the centre of the collimator.

(v) The spread in the incident electron beam energy E_0 is considered only by smoothing the calculated photon spectrum with a Gaussian of the respective width.

With these approximations Eq. (23) is reduced to a single integration over the electron angular distribution, subject to the condition that the radiated photons pass through the collimator

$$
\overline{I}^{co}(x) = \int d^2e\, w_{ED}(\underline{e}) I^{co}(\underline{x}, \underline{\Omega}_e = \underline{\Omega} + \underline{e})\bigg|_{r_\gamma < r_c}.
$$
(28)

4.2.1. Selection of lattice vectors

To shorten the calculation, only vectors with the strongest coherent contribution within the chosen volume of reciprocal lattice space $V_{\vec{g}}$ are included. The maximum contribution $I_{\vec{g}}^{co,max}$ of each lattice vector within $V_{\vec{g}}$ to the coherent intensity occurs at the corresponding discontinuity $x_d(\vec{g})$ and it is calculated using Eqs. (6a) and (7)

$$
I_{\vec{g}}^{co,max} = (1 + (1 - x_d)^2) \cdot 4G(\vec{g})\delta g_t^2/g_l^2.
$$
(29)

Note, that Ψ_2^{co} vanishes at x_d. Their relative importance depends on crystal orientation, but, in general out of typically 10^4 the 30 strongest contributions make up more than 99% of the total intensity; and they dominate the polarisation.

4.2.2. Effect of the electron angular distribution on the coherent spectrum

When the electron passes through the crystal at a different angle, the coherent intensity I^{co} is affected because the value g_l in Eqs. (7a–c) is modified (the corresponding, but fractionally smaller modification in g_t is evaluated using $g_t^2 = g^2 - g_l^2$). To obtain the uncollimated coherent spectrum (from Eq. (28) without the condition $r_\gamma < r_c$), the electron angle $\underline{e}$ is resolved into components, $e_\parallel$ in the $(\vec{g}, \vec{p}_0)$ plane and $e_\perp$ perpendicular to it. The change in g_l due to $e_\perp$ is of second order and can be neglected. The in-plane rotation $e_\parallel$ produces a change, $\Delta g_l = g_t \sin e_\parallel + g_l(1 - \cos e_\parallel)$ which can be approximated by $\Delta g_l = g_t e_\parallel$ because $e_\parallel$ is small. Inserting the Gaussian form of w_{ED}, carrying out the integral over $e_\perp$ and substituting $e_\parallel = \Delta g_l/g_t$, Eq. (28) simplifies to

$$
\overline{I}^{co} = \int_{\delta - g_l}^{g - g_l} d(\Delta g_l) \frac{1}{g_t \sigma_e \sqrt{2\pi}} \exp\left(-\frac{(\Delta g_l)^2}{2g_t^2 \sigma_e^2}\right)
$$
$$
\times I^{co}(x, g_l + \Delta g_l),
$$
(30)

in which the lower limit of integration reflects the pancake condition.

The functions Ψ^{co} which appear in I^{co} contain terms proportional to $1/g_l^n$ with $n = 0, 1, \ldots, 4$. To obtain an analytical form for the integral in Eq. (30) the Gaussian is approximated by a simpler function

$$
\frac{1}{g_t \sigma_e \sqrt{2\pi}} \exp\left(-\frac{(\Delta g_l)^2}{2g_t^2 \sigma_e^2}\right)
$$
$$
\approx \begin{cases} \dfrac{3}{4\sigma}\left(1 - (\Delta g_l/\sigma)^2\right) & \text{for } |\Delta g_l| \leqslant \sigma, \\ 0 & \text{for } |\Delta g_l| \geqslant \sigma, \end{cases}
$$
(31)

with $\sigma = \sqrt{5}g_t\sigma_e$ chosen to ensure that the *rms* width is the same for both distributions.

A further minor simplification is obtained by noting that $g_l \ll g$ except for the highest photon energies, so that the factor g_t^2 in the numerator of Eqs. (7a) and (7b) can be treated as constant. From Eq. (2) it follows that for the lowest lattice vector in diamond at $E_0 = 855$ MeV the ratio $(g_l/g)^2$ is 2×10^{-4} at $x = 0.5$ rising to 2×10^{-2} at $x = 0.9$ and still smaller values are obtained for higher lattice vectors or for higher electron energies. Carrying out the integrations in Eq. (30) one obtains with the help of Eq. (31)

$$
\overline{\Psi}_1^{co} = 3\sum_{\vec{g}} G\delta g_t^2 \frac{1}{\sigma^3}\left|(g_l^2 - \sigma^2)\frac{1}{f} + 2g_l \ln f - f\right|_{f=l_1}^{f=l_2},
$$
(32a)

$$\overline{\Psi}_2^{co} = 18 \sum_{\vec{g}} G\delta^2 g_t^2 \frac{1}{\sigma^3} \left| -(g_1^2 - \sigma^2)\frac{\delta}{3f^3} + \left(\frac{g_1^2}{2}\right.\right.$$
$$\left.\left. + g_1\delta - \frac{\sigma^2}{2}\right)\frac{1}{f^2} - (2g_1 + \delta)\frac{1}{f} - \ln f\right|_{f=l_1}^{f=l_2},$$
(32b)

$$\overline{\Psi}_3^{co} = -3 \sum_{\vec{g}} G\frac{\delta^3}{\sigma^3}\left[(g_2^2 - g_3^3)\cos 2\phi + 2g_2g_3\sin 2\phi\right]$$
$$\times \left|(g_1^2 - \sigma^2)\frac{1}{3f^3} - g_1\frac{1}{f^2} + \frac{1}{f}\right|_{f=l_1}^{f=l_2},$$
(32c)

where the limits are

$$l_1 = \max(\delta, g_1 - \sigma) \quad \text{and} \quad l_2 = \min(g, g_1 + \sigma).$$
(33)

Note, the definition of l_1 reflects the pancake condition.

4.2.3. Collimation

As a result of the energy–angle relation, which applies only to the coherent photon spectrum, the effect of collimation on the coherent and incoherent spectra is quite different. However, both cases can be treated in terms of the same collimation function $C(U)$, which is defined as the fraction of photons emitted at an angle U to the axis of the photon cone that pass through the collimator. In the coherent spectrum the effect of collimation at angle U_c is to remove photons with energies less than x_c given by Eq. (14). If the effects of beam spot size, beam divergence and multiple scattering are ignored, the cutoff at x_c is sharp. However, these processes produce an angular spread of the coherent photon cone direction with respect to the collimator, which is described here by a Gaussian distribution $w_{CB}(\rho)$, and this smears out the lower edge of the coherent peak at x_c. When treating this smearing, it is a reasonable assumption that all electrons produce the same photon energy spectrum $\overline{I}^{co}(x)$ and that the same energy–angle relation, $U(x)$ (Eq. (11)) and the value of x_d (Eq. (4a)) apply for all electron angles. This is justified because the main effect of the electron angular distribution on the photon spectrum $\overline{I}^{co}(x)$ is a smearing of the upper edge at energy x_d. With this assumption the collimated energy spectrum can be written

$$I_{\text{ANB}}^{co}(x) = \overline{I}^{co}(x) \cdot C(U(x)).$$
(34)

The collimation function $C(U)$ is obtained by integrating the distribution $w_{CB}(\rho) = (1/2\pi\sigma_c^2) \exp(-\rho^2/2\sigma_c^2)$ over ρ and ξ subject to the condition to be satisfied if the photon is accepted, viz.

$$U^2 + \rho^2 - 2\rho\cos\xi \leqslant U_c^2,$$
(35)

in which ρ is the angular offset of the photon cone from the collimator centre and ξ is the azimuthal angle between the photon plane and the offset plane. The result is
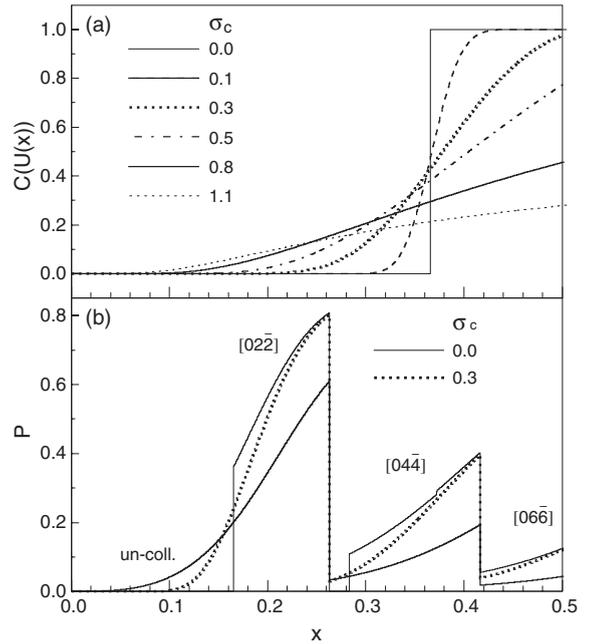

Fig. 7. (a) Collimation function $C(U(x))$ versus x for several variances σ_c to account for beam divergence, multiple scattering and finite beam spot size. The upper edge of the coherent peak is at $x_d = 0.5$ and the collimation angle $U_c = 0.94$ resulting to $x_c \sim 0.365$. (b) The influence of collimation at $U_c = 0.94$ on the polarisation is shown including all these experimental effects for $\sigma_c = 0.3$ (dotted line). It is compared to the uncollimated case for $\sigma_c = 0.3$ (thick solid) and the ideal collimated (thin solid) case with $\sigma_c = 0.0$. The kink in the $\sigma_c = 0.0$ case at $x = 0.37$ originates from the collimation discontinuity of the lattice vector $[0\,6\,\bar{6}]$.

$$C(U) = \Theta(U_c - U)\left[1 - \exp\left(-(U_c - U)^2/2\sigma_c^2\right)\right]$$
$$+ \int_{|U_c - U|}^{U_c + U} \rho\, d\rho \frac{1}{\sigma_c^2} \exp\left(-\rho^2/2\sigma_c^2\right)$$
$$\times \frac{1}{\pi} \arccos\left(\frac{\rho^2 + U^2 - U_c^2}{2\rho U}\right). \tag{36}$$

A numerical integration of the second term in Eq. (36) has to be carried out for a range of values of U and the energy–angle relation $U(x)$ is then used to determine the energy dependence $C(U(x))$.

The energy dependence of the collimated incoherent bremsstrahlung spectrum $I_{ANB}^{in}(x)$ is obtained by integrating the product of the Schiff spectrum $(dI^S/d(U^2))(U, x)$ (Eq. (16)) and $C(U)$ over all photon angles U. After integrating by parts this can be expressed in terms of the integrated-to-angle-U Schiff spectrum $I^S(U, x)$ (Eq. (19))

$$I_{ANB}^{in}(x) = \int dv\, c(v) I^S(v, x),$$

with

$$c(v) = \frac{1}{2v\sqrt{v - v^2}} \frac{dC(U)}{dU}, \tag{37}$$

where $v = 1/(1 + U^2)$, $C(U(x))$ and $c(v)$ have to be calculated numerically only once and the remaining evaluation of the intensities is a closed analytical calculation (apart from the ES folding) providing results very fast at only a tiny loss of accuracy.

The collimation function $C(U(x))$ is plotted in Fig. 7(a) for a fixed collimation angle $U_c = 0.94$ and $x_d = 0.5$ and for several values of the variance σ_c. The resulting $x_c \sim 0.365$ and the increase in diffuseness with increasing σ_c is evident. In Fig. 7(b) the effect of collimation on the polarisation is demonstrated. For the ideal case with no additional
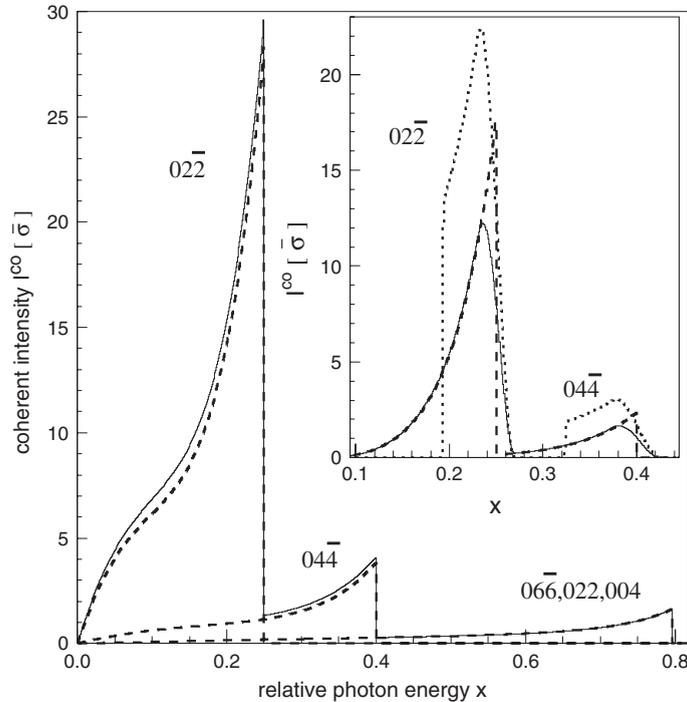

Fig. 8. Monte Carlo calculations (ANB) of the coherent intensity for the electron beam and crystal parameters given in Table 1, set A. The uncollimated spectrum is calculated with zero beam divergence and beam spot size, and the largest contributions from the $[0\,2\,\bar{2}]$, $[0\,4\,\bar{4}]$ and the sum of the $[0\,6\,\bar{6}]$, $[0\,2\,2]$ and $[0\,0\,4]$ lattice vectors are shown by the three dashed lines; the solid line is the total intensity. For the collimated case, the insert shows the individual effects of BS and ED (= BD + MS) on the discontinuity regions x_c and x_d: ED on x_d (dotted line), BS + ED on x_c (dashed line) and BS + ED on x_c and x_d (solid line).

angular spreading (solid thin line), the collimation cuts off the intensity below x_c for each of the lattice vectors. The degree of polarisation is increased compared to the uncollimated case (solid thick line) due to the different angular distributions of coherent and incoherent processes. Multiple scattering, electron divergence and beam spot size modify the polarisation around the lower discontinuities x_c as demonstrated by the dotted line which results from a calculation with $\sigma_c = 0.3$.

Specific contributions to the spectra and the effects of particular processes can be studied in detail. For example, Fig. 8 contains results from an ANB calculation of the coherent contributions to the photon intensity produced by a 855 MeV electron beam (parameters from Table 1, set A). The three most dominant contributions, which are due to the lattice vectors $[0\,2\,\bar{2}]$, $[0\,4\,\bar{4}]$ and the triple of $[0\,6\,\bar{6}]$, $[0\,2\,2]$ and $[0\,0\,4]$, are shown for a calculation assuming vanishing variances for beam spot size and divergence. The dashed lines show the individual contributions which all extend to low photon energies. At the maximum of the dominant $[0\,2\,\bar{2}]$ intensity the other lattice vectors contribute about 5% to the total (full line). The effects of beam divergence and beam spot size are best visible for collimated intensities (see insert of Fig. 8). Collimation of an ideal beam leads to sharp structures bounded by x_c on the low and x_d at the high-energy side. The insert demonstrates the effects due to realistic beam conditions separately for both x_c and x_d: the smearing by BD and MS around the discontinuity x_d is shown by the dotted line and the dashed curve demonstrates the modification of the intensity around the lower cutoff x_c due to BS, BD and MS. All these effects combined (full line in insert) decrease the coherent intensity and thus the polarisation and to some extent reduce the advantage gained by collimation.

5. Results

Before discussing applications, a comparison of results from the two codes is presented in Fig. 9 for the cases of an uncollimated photon beam (left panel) and a collimated beam (right panel). The calculations were performed for a typical experimental condition at MAMI with $E_0 = 855$ MeV, with the upper edge of the main coherent peak placed at 220 MeV. The parameters of the beam and of the radiator are summarised in Table 1, set A. Coherent and incoherent intensities calculated by MCB are shown as histograms in Fig. 9(a) and (b). The differences of $\leqslant 1\%$ between the MCB and ANB results would be barely visible; the only significant differences between the coherent intensities occur at the highest photon energies, because the number of higher order lattice vectors in ANB is reduced to 30 for computational speed (12 h for MCB versus 2 min for ANB). The incoherent intensities from the diamond crystal ($Z = 6$) are given with (dashed) and without electron contribution (solid line). For an amorphous nickel radiator ($Z = 28$) the difference is less pronounced as shown by the dot-dashed and dotted lines in Fig. 9(a).

The respective polarisations calculated with MCB are shown in Fig. 9(c) and (d). The negative contribution at the very high photon energies arises through the restriction of lattice vectors taken into account. The agreement of the polarisations from the two codes is as good as would be expected given the agreement between the coherent intensities. The polarisation, by itself proportional to a difference of polarised cross sections, is particularly sensitive to approximations at the discontinuities which is bourne out in the difference spectra as shown in Fig. 9(e) and (f). The differences between the codes are more pronounced for

Table 1
Parameters for calculations of bremsstrahlung spectra at different electron energies E_0 and crystal orientations (Θ, α)

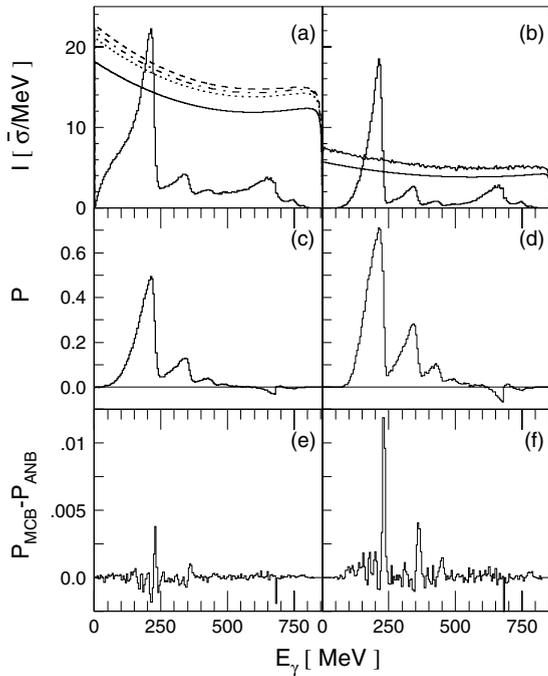| Set	E_0, MeV	Θ, rad	α, rad	σ_x, mm	a_y, mm	σ_{ax}, mrad	σ_{ay}, mrad	z_R, mm	θ_c, mrad
A	855	0.0607	0.694	0.2	0.06	0.084	0.084	0.1	0.564
B	855	0.0607	0.662	0.2	0.06	0.084	0.084	0.1	0.564
C	855	0.0607	0.600	0.2	0.06	0.084	0.084	0.1	0.564
D	1160	0.1501	0.8179	0.1	0.1	0.39	0.39	1.1	1.13
E	25,300	0.03	0.77	1.0	1.0	0.01	0.01	0.1	∞

Fig. 9. Spectra calculated with parameter of set A of Table 1 by MCB (histogram) for uncollimated (left panel) and collimated (right) conditions, (a) and (b) coherent and incoherent intensity distributions, (c) and (d) polarisation spectra, (e) and (f) difference in polarisation between MCB and ANB.

the collimated case (right panel) than for the uncollimated one. They are largest at x_d where they amount to less than 3% of the maximum polarisation while they reach less than 1% elsewhere. It can be concluded that both codes produce spectra of the same quality for the present experimental conditions.

The advantage of having all observables available in the MCB code is demonstrated by a two-dimensional plot of the polar and azimuthal angular variation of the photon intensities (Fig. 10). This distribution shows clearly a $\cos^2 \phi_k$ dependence and is instructive for the design of photon collimators. For a circular collimator the chosen radius is a compromise between cutting out valuable coherent yield at some azimuth and accepting incoherent at others. Here, we have used the realistic values from the Mainz experiment, where a collimator of length $l_c = 200$ mm and radius $r_c = 1.5$ mm had been positioned at a distance of

$z_c = 2.5$ m. The respective polar angle is indicated by a horizontal line in Fig. 10(a). A rectangular collimator (dotted line) might achieve a higher polarisation, although it would have to be rotated by 90° each time the polarisation was rotated by 90° (this is done frequently during measurements to reduce systematic errors). Fig. 10(d) shows that the improvement in the polarisation is not significant except where its magnitude is already low. The effect of misalignment (horizontal shift by 1 mm) of the same circular collimator is also shown. It primarily reduces the photon flux and photon polarisation.

A comparison of the ANB calculations to the experimental spectra has been given already in Fig. 1, and Fig. 9 shows that the MCB code gives almost identical results for these spectra. The amorphous (incoherent) bremsstrahlung spectrum on nickel (Fig. 1(a)) as well as the total spectrum on a 100 μm diamond (Fig. 1(b)) are soundly described by ANB over the whole measured photon range from 40 to 800 MeV. The ratio of these spectra (Fig. 1(c)) is more sensitive to details of the coherent contribution and the calculation does show failings at the highest photon energies due to a restricted number of lattice vectors, but the region of the highest polarisation around the dominant lattice vector $[0\,2\,\bar{2}]$ is well described.

In Fig. 11 comparison is made between ANB calculations and four measurements of the crystal intensity spectra I^{cr}. Three were obtained during "tagging efficiency" measurements in a $^4\mathrm{He}(\vec{\gamma}, np)$ experiment at Mainz and the fourth is from the TAGX facility [28] which used a thicker crystal and had a larger beam divergence than available at Mainz. The respective parameters are listed in Table 1, sets A–D. In each case the complete spectra are described well. The findings provide confidence that all essential effects have been accounted for.

Measurement of the polarisation of a photon beam is a difficult task and only one measurement [6] exists that can be used to check the calculations of P. This was made at photon energies around $E_\gamma \sim 300$ MeV using the coherent $^4\mathrm{He}(\vec{\gamma}, \pi^0)$ reaction which has a known photon asymmetry, $\Sigma = 1.0$. The results for two different collimation
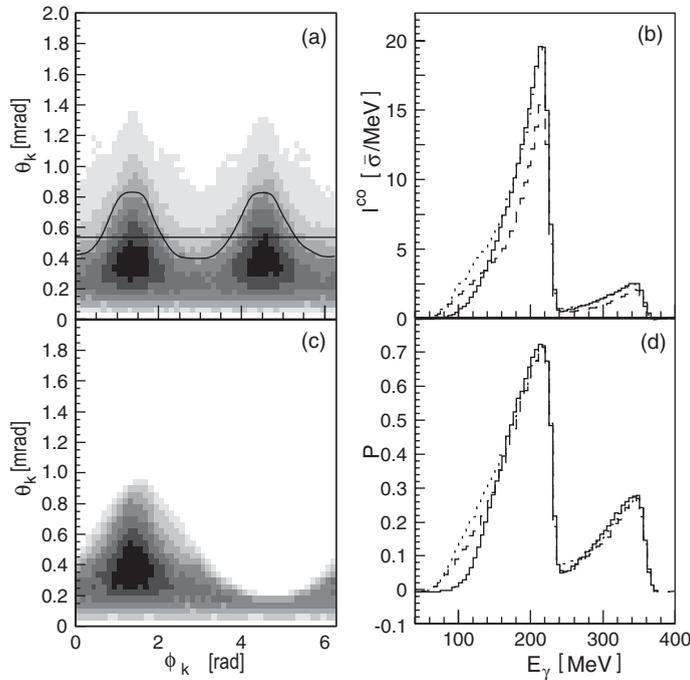
Fig. 10. (a) Predicted intensity distribution versus the polar and the azimuthal photon angle for coherent bremsstrahlung production in a diamond crystal. The lines correspond to the limits due a circular and rectangular collimator. (c) The effect of an off-centred collimator is shown. The intensity spectra and the polarisations are plotted in panels (b) and (d): circular collimator (full line), rectangular collimator (dotted line), off-centred collimator (dashed lines).

angles $\vartheta_c = 0.5$ mrad (Fig. 12(a)) and $\vartheta_c = 0.7$ mrad (Fig. 12(b)) are compared to ANB calculations and good agreement is obtained. In the present calculations this agreement follows from using measured beam parameters, whereas in the earlier calculations reported in [6] it was necessary to increase the beam divergence by a factor 2 to obtain agreement. Fig. 12 shows that a 10% increase is gained using the smaller collimator, but only at the expense of a considerable reduction in intensity, which is responsible for doubling the error bars in the polarisation.

Fig. 13 presents calculations of the crystal intensity spectra I^{cr} and polarisations P which can be expected in three future facilities using coherent bremsstrahlung on a diamond. The electron energies are $E_0 = 1.5$ GeV (MAMI C), 6 GeV (Jefferson Lab) and 25.3 GeV (ELFE). In general, the degree of polarisation available increases slowly with electron energy.

5.1. Study of sensitivity

The photon polarisation depends on the electron beam properties and on the thickness and the angular positioning of the crystal. To determine the precision required in the values of these parameters, the sensitivity of the polarisation to each parameter was estimated. A set of nominal experimental parameters corresponding to the conditions at MAMI B was chosen, which produce a coherent peak with its cutoff at $E_\gamma = 220$ MeV. These parameters correspond to set A of Table 1 and are listed as X_i^0 in Table 2. The polarisation spectrum was calculated for the nominal values X_i^0 and for a sample of surrounding values changing only one parameter each time. For each spectrum an average polarisation $\overline{P}$ was calculated in the region between the upper cutoff x_d of the peak and the lower energy at which the polarisation fell to half its maximum value. The results are presented
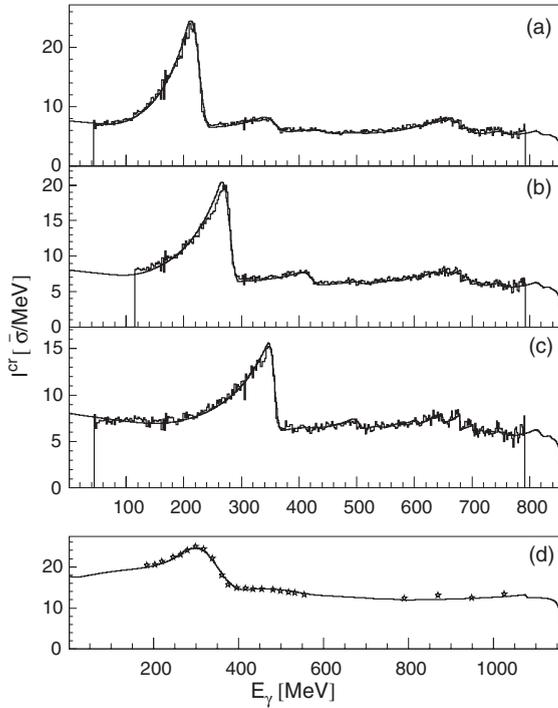
Fig. 11. Comparison of total crystal intensities I^{cr} calculated with ANB to experimental spectra, (a)–(c) taken from measurements at MAMI during the ^{4}He($\vec{\gamma}$,np) experiment (Table 1, set A–C) and (d) from TAGX [28] (Table 1, set D).
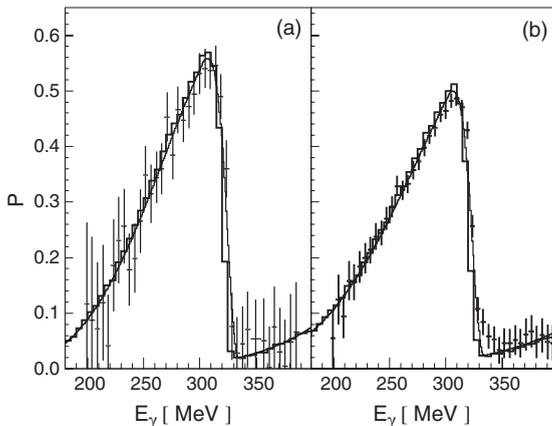

Fig. 12. Linear polarisation from the ANB calculation with MAMI-beam parameters for $E_\gamma = 300$ MeV (a) for the collimation angle $\vartheta_c = 0.5$ mrad and (b) $\vartheta_c = 0.7$ mrad in comparison with a measurement of the asymmetry of coherent π^0 photoproduction from ^{4}He [6].

in Table 2 as the absolute change ΔX_i, which produces a 1% relative change in $\overline{P}$.

The polarisation shows strongest sensitivity to the angular settings of the crystal, but even so the corresponding precision required for the vertical and horizontal rotations of the goniometer is only ≈ 0.1 mrad, which is readily achieved. A similar accuracy in mounting the crystal is not necessary, since the angular offsets are determined in initial calibrations. The thickness of the diamond is only important when a narrow collimator is used and even then the required precision is not demanding. At Mainz, because the beam phase space is small, the polarisation is not much affected by the beam spot size and the beam divergence only begins to have a large influence if narrow collimation is used.

These comments are of course only appropriate for the specific conditions, which have been found for the experiments with coherent bremsstrahlung at Mainz. The conclusions are likely to be different for radiators of very different thickness or for different beam energies or qualities.

One parameter not mentioned above but crucial if high polarisation is to be obtained, is the structure of the crystal. The structure must not change over the part of its volume sampled by the electron beam. For the MAMI experiments suitable high quality crystals, which satisfy this condition, have been selected by X-ray scattering measurements. No attempt has been made to incorporate the possible effects of crystal imperfections into the MCB or ANB codes.

5.2. Polarisation extracted from yield

It is rarely possible to measure the photon polarisation in parallel to the actual experiment; usually it is extracted from offline analysis of the data. As discussed above, during so-called "tagging efficiency runs" a lead glass scintillator in coincidence with the tagging spectrometer measures the cross section as function of photon energy. To determine the photon polarisation within the standard procedure, the incoherent part of the measured bremsstrahlung spectrum on a diamond is subtracted by substituting it directly with the amorphous spectrum from a nickel radiator.
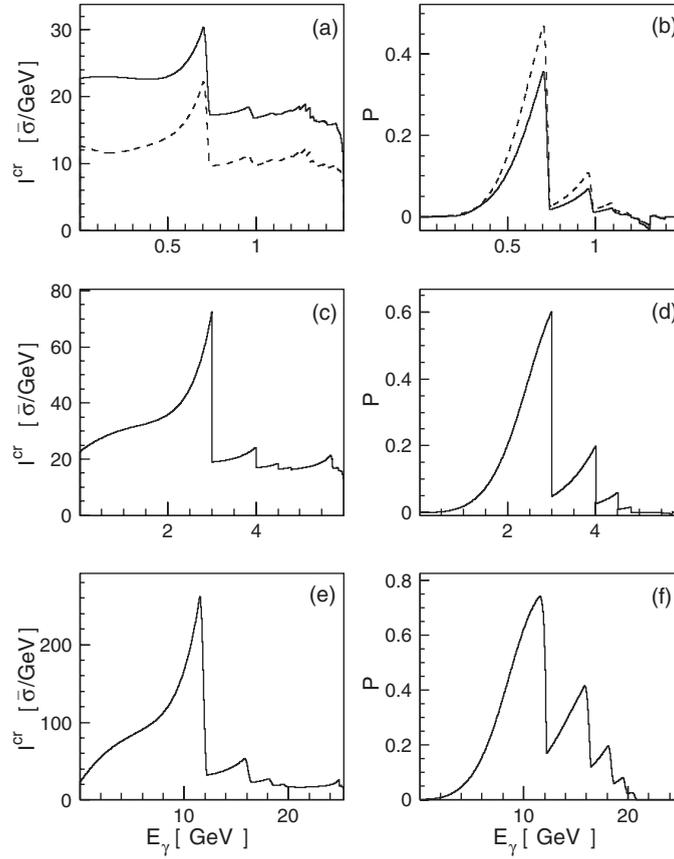
Fig. 13. Predictions of the uncollimated crystal intensities and polarisations to be expected at the accelerators MAMI C for $E_e = 1.5$ GeV, Jefferson Laboratory ($E_e = 6$ GeV) and ELFE ($E_e = 25.3$ GeV). The dashed lines in panels (a) and (b) show results for MAMI C with collimation of $U_c^2 = 0.9$.

Table 2
Sensitivity of the calculated average polarisation $\overline{P}$ to various experimental parameters X_i for three different collimator diameters (r_c) and the uncollimated situation ($r_c = \infty$)

| X_i | X_i^0 | r_c/mm | | | |
		1.5	2.5	4.0	∞
Θ	60.7 mrad	3.4	3.4	3.4	3.4
α	694 mrad	5.9	5.2	4.9	4.6
z_R	100 μm	14	50	250	200
σ_{sx}	0.20 mm	0.67	1.00	2.00	–
σ_{sy}	0.06 mm	0.20	0.30	0.60	–
$\sigma_{ax,ay}$	160 μrad	34	123	229	–
z_c	2.5 m	0.23	0.15	0.28	–

The deviations ΔX_i which cause an uncertainty of $\Delta\overline{P}/\overline{P} = 0.01$ are listed.

Further analysis relies on the calculations, and from the agreement for the structures in the coherent part the excellence of the calculated polarisation is inferred. This method was used so far for most of the analyses of experiments with linearly polarised photons at Mainz.

Three more precise procedures are indicated below, all of them rely on accurate calculations of the various contributions. The first one uses only the cross section σ_D^{exp} measured with the diamond crystal. The polarisation P_Y can be extracted online by help of model calculations through expanding the basic Eq. (1) with $\sigma^{co} = \sigma^{cr} - \sigma^{in} - \sigma^{el}$ and rearranging

$$P_Y = \frac{\sigma^{dif}}{\sigma^{cr}} \cdot \frac{\sigma^{cr} - \sigma^{in} - \sigma^{el}}{\sigma^{co}}$$
$$= \frac{\sigma^{diff}}{\sigma^{co}} \cdot \frac{\sigma_D^{exp} - \sigma^{in} - \sigma^{el}}{\sigma_D^{exp}}, \tag{38}$$

where on the r.h.s only σ^{cr} is replaced by σ_D^{exp} while the other cross sections are taken from the calculations. The success of this method depends on the quality of the description of the measured spectrum and the fact that σ^{dif} as well as σ^{co} are related to the crystal structure. The results of this procedure are shown in Fig. 14. In the upper figure the coherent cross section $\sigma_Y^{co} = \sigma^{exp} - \sigma^{in} - \sigma^{el}$ (full line) is compared to a calculation (dashed line), whereas in the lower figure the respective polarisations have been plotted. The experimental intensity spectrum is produced within a 220 MeV run at MAMI. The calculation with slightly different crystal orientation was performed in order to demonstrate that slight misalignments still produce accurate polarisations. The agreement between the two polarisations is excellent. Only above the discontinuity the contributions of other lattice vectors cause a difference, but this region in general is not considered for analysis.

This first method can be used offline for the collimated photon spectra and also online for the uncollimated ones. The tagging spectrometer provides the free-running rates of the focal plane detectors and thus the uncollimated photon spectrum. In the latter case the calculation has also to account for the effects of collimation, however, the data are being taken in a single run which reduces systematic uncertainties, particularly the one arising from the normalisation at extremely low beam intensities.

The second method relies on collimated spectra which are obtained from tagging efficiency runs for diamond crystals as well as for amorphous radiators. This time also the incoherent contribution is replaced by measured yields after corrections for electronic contributions and for other differences in the radiators

$$P_T = \frac{\sigma^{dif}}{\sigma^{co}} \cdot \frac{\sigma_D^{exp} - \sigma_{Ni}^{exp} \cdot f}{\sigma_D^{exp}}, \tag{39}$$

with

$$f = 1 - \left(\frac{(\sigma^{am} + \sigma_{Ni}^{el}) - (\sigma^{in} + \sigma_D^{al})}{\sigma^{am} + \sigma_{Ni}^{dif}} \right).$$

Note, that proper choice of the radiator thicknesses makes f close to 1 because the cross section pairs $(\sigma^{am}, \sigma^{in})$ and $(\sigma_{Ni}^{el}, \sigma_D^{el})$ cancel each other roughly due to their similarity in shapes.

Even better cancellation can be achieved by using the same diamond crystal, however in such orientation to not produce any coherent contribution in the region of interest. A study of this third method, which uses only one radiator, however in two orientations, will be reported in a forthcoming paper.

The advantage of using uncollimated data (i.e. the electron rates in the focal plane detectors) rests in the high rates observed in free-running electron counters and thus in high statistical accuracy. Collimated photon spectra resemble the flux in the reaction target more closely; their benefit is slightly reduced by the fact, that the data are taken at different exposure times and at possibly different electron intensities. However, the combined overall agreement of indirect and direct determination of polarisation gives high confidence in the suggested methods.
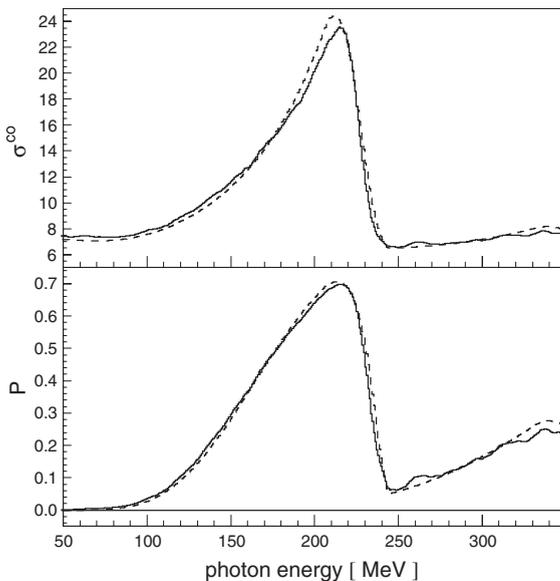

Fig. 14. Results of the ratio method. Top: the experimental coherent cross section $\sigma_Y^{co} = \sigma_D^{exp} - \sigma^{in} - \sigma^{el}$ (full line), deduced from the measured σ_D^{exp} and a model calculation. Bottom: the polarisation P_Y is plotted, see Eq. (38). Both are compared with a model calculation (dashed lines).

6. Summary

The calculation of bremsstrahlung spectra from amorphous radiators and lattices has been greatly

improved. This was achieved by accounting properly for angular and Z dependences of the basic processes. The new analytical code permits quick studies of symmetric cases at a small loss of precision. For non-symmetric conditions or final configurations, the Monte Carlo provides the full precision from calculations without approximations. Due to the list-mode type output the collimation studies can be performed without repeating the time consuming calculations themselves.

Finally, excellent agreement with the photon spectra measured under varying conditions at different laboratories was achieved. This fact permits the extraction of the polarisation of the photon beam from the intensity spectra themselves and its use in experiments. The sensitivity to crystal orientation and thickness has been examined.

Acknowledgements

References

[1] E.J. Williams, Phys. Rev. 45 (1934) 729.
[2] H. Überall, Phys. Rev. 103 (1956) 1055, Phys. Rev. 107 (1957) 223.
[3] G. Diambrini Palazzi, Rev. Mod. Phys. 40 (1968) 611.
[4] U. Timm, Fortschritte Phys. 17 (1969) 765.
[5] D. Lohmann et al., Nucl. Instr. and Meth. A 343 (1994) 494;
    D. Lohmann, Diploma Thesis, Göttingen University, 1992.
[6] F. Rambo et al., Phys. Rev. C 58 (1998) 489;
    F. Rambo, Diploma Thesis, Göttingen University, 1995.
[7] I. Anthony, J.D. Kellie, S.J. Hall, G.J. Miller, J. Ahrens, Nucl. Instr. and Meth. A 301 (1991) 230.
[8] H. Herminghaus, K.H. Kaiser, U. Ludwig, Nucl. Instr. and Meth. A 187 (1981) 103.
[9] M.M. May, Phys. Rev. 84 (1951) 265.
[10] L.C. Maximon, A. De Miniac, T. Aniel, E. Ganz, Phys. Rep. 147 (1987) 190;
    H. Olson, L.C. Maximon, Phys. Rev. 114 (1959) 887.
[11] W. Heitler, Quantum Theory of Radiation, Oxford University Press, London, 1964.
[12] W. Greiner, J. Reinhardt, Theoretische Physik, Bd.7, Quantenelektrodynamik, Harri Deutsch – Thun, Frankfurt (Main), 1984.
[13] F.A. Natter, in: Proceedings of the 4th Workshop on Electromagnetically Induced Two-Hadron Emission, Granada, May 1999.
[14] F.A. Natter, Internal Report 98/1, Tübingen 1998, unpublished;
    S. Wunderlich, Internal Report 97/1, Tübingen 1997, unpublished;
    http://pit.physik.uni_teubingen.de/grabmayer/publications.html.
[15] H.W. Koch, J.W. Motz, Rev. Mod. Phys. 31 (1959) 920.
[16] J.A. Wheeler, W.E. Lamb, Phys. Rev. 55 (1938) 858.
[17] L. Criegee, M. Garrell, H. Sadrozinski, U. Timm, W. Zimmermann, Phys. Lett. B 28 (1968) 140.
[18] R.F. Mozley, J. DeWire, Nuovo Cimento 27 (1963) 1281.
[19] D.T. Cromer, J.T. Waber, Acta Cryst. 18 (1965) 104.
[20] E.N. Maslen, A.G. Fox, M.A. O'Keefe, in: A.J.C. Wilson (Ed.), International Tables for Crystallography, Tabs. 6.1.1.4 and 6.1.1.5, Kluwer Academic Publishers, Dordrecht, 1992.
[21] L.I. Schiff, Phys. Rev. 83 (1951) 252.
[22] J.H. Hubbell, J. Appl. Phys. 30 (7) (1959) 981.
[23] W.H. Press, S.A. Teukolsky, W.T. Vetterling, B.P. Flannery, Numerical Recipes in C, Cambridge University Press, 1992.
[24] J.L. Matthews, R.O. Owens, Nucl. Instr. and Meth. 111 (1973) 157.
[25] G. Molière, Z. Naturforsch. 3a (1948) 78.
[26] H.A. Bethe, Phys. Rev. 89 (1953) 1256.
[27] A.I. Akhiezer, N.F. Shul'ga, V.I. Truten', A.A. Grinenko, V.V. Syshchenko, Sov. Phys.-Usp. 38 (1995) 1119;
    N.F. Shul'ga, V.I. Truten', S.P. Fomin, Radiat Eff. 91 (1986) 179.
[28] T. Suda for the TAGX collaboration, in: K. Maruyama, H. Okuno (Eds.), Proceedings of the International Symposium on Hadron and Nuclear Physics with Electromagnetic Probes, Elsevier, Amsterdam, 2000.